GaN: From three- to two-dimensional single-layer crystal and its multilayer van der Waals solids

A. Onen,[1,2] D. Kecik,[1] E. Durgun,[1,2,*] and S. Ciraci[3,†]

[1]*UNAM-National Nanotechnology Research Center, Bilkent University, Ankara 06800, Turkey*

[2]*Institute of Materials Science and Nanotechnology, Bilkent University, Ankara 06800, Turkey*

[3]*Department of Physics, Bilkent University, Ankara 06800, Turkey*

(Received 2 December 2015; published 19 February 2016)

Three-dimensional (3D) GaN is a III-V compound semiconductor with potential optoelectronic applications. In this paper, starting from 3D GaN in wurtzite and zinc-blende structures, we investigated the mechanical, electronic, and optical properties of the 2D single-layer honeycomb structure of GaN (g-GaN) and its bilayer, trilayer, and multilayer van der Waals solids using density-functional theory. Based on high-temperature *ab initio* molecular-dynamics calculations, we first showed that g-GaN can remain stable at high temperature. Then we performed a comparative study to reveal how the physical properties vary with dimensionality. While 3D GaN is a direct-band-gap semiconductor, g-GaN in two dimensions has a relatively wider indirect band gap. Moreover, 2D g-GaN displays a higher Poisson ratio and slightly less charge transfer from cation to anion. In two dimensions, the optical-absorption spectra of 3D crystalline phases are modified dramatically, and their absorption onset energy is blueshifted. We also showed that the physical properties predicted for freestanding g-GaN are preserved when g-GaN is grown on metallic as well as semiconducting substrates. In particular, 3D layered blue phosphorus, being nearly lattice-matched to g-GaN, is found to be an excellent substrate for growing g-GaN. Bilayer, trilayer, and van der Waals crystals can be constructed by a special stacking sequence of g-GaN, and they can display electronic and optical properties that can be controlled by the number of g-GaN layers. In particular, their fundamental band gap decreases and changes from indirect to direct with an increasing number of g-GaN layers.

DOI: 10.1103/PhysRevB.93.085431

I. INTRODUCTION

The excellent electronic and optical properties of gallium nitride crystal in wurtzite structure (wz-GaN) have made it an important semiconductor with critical and wide ranging technological applications in microwave communications, lasers, detectors, light-emitting diodes in the ultraviolet range, etc. [1,2]. It has ∼3.4 eV direct band gap and exhibits high chemical, thermal, and mechanical stability, which is convenient for various applications such as nanoelectromechanical systems (NEMS). Additionally, GaN and similar III-V compounds such as AlN can form heterostructures with commensurate interfaces, which offer interesting quantum structures in lower dimensionality and display unusual device properties. In addition, three-dimensional (3D) GaN crystal can be grown easily by various methods, whereby the fabrication of thin films and heterostructures is achieved. However, so far single-layer (SL) GaN has not been synthesized yet.

Searching the contender of semimetallic graphene in the field of 2D electronics and in other potential applications has brought semiconductors such as silicon and GaAs into focus. Earlier, the optimization of SL silicon and GaAs structures from first principles indicated that they can be stable in a SL buckled honeycomb structure [3]. Furthermore, while silicon in a buckled honeycomb structure, which is called *silicene*, is a semimetal with bands crossing linearly at the Fermi level, SL GaAs was found to be a semiconductor [3]. Later, theoretical studies using first-principles phonon and high-temperature molecular-dynamics (MD) calculations within density-functional theory (DFT) demonstrated the stability of silicene and germanene (i.e., SL buckled honeycomb structure of germanium) [4,5], which are isovalent with graphene. Moreover, in a different study, it was predicted that IV-IV and III-V compounds [6,7] and also group II-VI compounds [8], with constituent elements having s^2p^m valence orbitals, can form stable, graphenelike SL honeycomb structures with a 2D hexagonal lattice. It was surprising that even if several of these SL honeycomb structures did not have layered 3D parent crystals such as graphite or h-BN, some of the predictions of the theoretical studies were realized experimentally. For example, silicene, germanene [9,10], and a very thin layer of AlN [11], etc., were synthesized. In view of the recent advances in growth techniques and experiences developed through the fabrication of GaN thin films, it is expected that the growth of a SL honeycomb structure of GaN, i.e., g-GaN, will be achieved soon. Given the role of wz-GaN in device technology, the growth of g-GaN would have a real impact in 2D flexible nano-optoelectronics.

While the positive phonon frequencies in the previous study [6] indicates stability against small displacements, stability at high temperature was not assured. Therefore, the main task of this paper is to show that g-GaN corresponds to a deep, local minimum on the Born-Oppenheimer (BO) surface and hence remains stable at high temperature. Having proven the stability, we performed a comprehensive and comparative study using DFT on 3D wz-GaN and its allotrope in cubic zinc-blende structure, namely zb-GaN, as well as on a SL honeycomb structure together with its multilayers. Our main objective is to reveal whether g-GaN can replace 3D wz-GaN in 2D electronics. We will clarify how the physical properties—particularly elastic, electronic, and optical properties—can change as the dimensionality varies from 3D

*durgun@unam.bilkent.edu.tr

†ciraci@fen.bilkent.edu.tr

to strictly 2D. In the past, the physical properties, particularly the electronic energy structure of 3D wz-GaN and zb-GaN, have been treated by using methods similar to the one used in this study. In a majority of these studies, the calculated band gaps of wz-GaN and zb-GaN were underestimated by almost 1.7 eV when compared to the experimental values. While this discrepancy between the DFT band gap and the experimental value is well known, improving the theoretical predictions of band gaps has been a primary motivation in recent studies, including ours. Other objectives of our study have been to explore the following: (i) Can bilayer, trilayer, and periodic multilayer structures be constructed by stacking of g-GaN? (ii) How do their physical properties vary with the number of layers? (iii) Can a suitable substrate be deduced to grow g-GaN, and can the properties of g-GaN predicted in this study be modified when it is grown on this substrate?

Important results of our study are summarized as follows: (i) Large discrepancies between the experimentally determined fundamental band gap of 3D GaN crystals and DFT results can be overcome by applying corrections. Such corrections appear to be necessary also for g-GaN. (ii) *Ab initio* MD calculations proved that the honeycomb-like structure remains stable at temperatures as high as 1000 K. (iii) In 2D g-GaN structure, the fundamental band gap increases and becomes indirect. Relative to the parent 3D crystals, the optical-absorption spectrum of g-GaN is modified significantly. (iv) When grown on semiconducting blue phosphorene, which is lattice-matched, the physical properties of the freestanding g-GaN are preserved. In this respect, layered blue phosphorus can be an ideal substrate to grow g-GaN. (v) g-GaN can form a stable bilayer, as well as multilayers, where the interlayer binding occurs through chemical and van der Waals (vdW) interaction. The fundamental gap is altered with the number of layers; it decreases and is converted from indirect to direct gap as the number of layers increases. The amplitude and onset energy of the absorption spectrum can be controlled by the number of layers in the g-GaN multilayers. Finally, a 3D layered periodic structure of GaN-like graphite can be constructed artificially by stacking g-GaN.

II. COMPUTATIONAL METHODOLOGY

First-principles calculations were performed in order to investigate the ground-state properties of bulk and 2D g-GaN within spin-polarized density functional theory (DFT). The projector-augmented-wave potential (PAW) formalism [12] implemented in the Vienna Ab-initio Simulation Package (VASP) [13–16] was used. The electron exchange and correlation potential was described by the Perdew-Burke-Ernzerhof (PBE) form within the generalized gradient approximation (GGA), where d electrons are also taken into account (GGA-d XC potential) [17,18]. The plane-wave basis set was defined by an energy cutoff at 520 eV for all calculations. Moreover, the van der Waals interactions were taken into account for the layered structures [19,20]. Atomic positions were optimized using the conjugate gradient (CG) method; the total energy and atomic forces are minimized with an energy difference between the sequential steps set to 10^{-5} eV for convergence. The maximum allowed force on each atom and the Gaussian smearing factor were taken as 0.05 eV/Å and 0.05 eV, respectively. A Γ-centered $35 \times 35 \times 1$ mesh was used for the Brillouin zone integrations of the primitive unit cell. To avoid spurious interactions between the periodic images, a supercell with $\sim$20 Å vacuum space was adopted. The cohesive energies of 3D and 2D GaN allotropes are calculated from the expression $E_c = E_T(\mathrm{Ga}) + E_T(\mathrm{N}) - E_T(\mathrm{GaN})$ in terms of the total energies, $E_T(\mathrm{Ga})$ and $E_T(\mathrm{N})$, of free Ga and N atoms and the optimized total energy, $E_T(\mathrm{GaN})$, of a specific allotrope. The higher the positive E_c, the stronger is the binding. An interionic charge-transfer analysis between Ga and N was carried out for the bulk and g-GaN using the Bader charge-analysis method [21].

In addition to *ab initio* phonon calculations [22,23], the stability of the structures was tested at high temperatures by *ab initio* molecular-dynamics (MD) calculations using two different approaches. In the first one, a Nosé thermostat [24] was used and Newton's equations were integrated through a Verlet algorithm with a time step of 1 fs. In the second one, we scaled the velocities at each time step in order to keep the temperature constant.

Subsequent to the standard-DFT results, hybrid functionals (HSE06) [25–27] and quasiparticle (QP) G_0W_0 corrections [28–30], where G and W were iterated once, were undertaken in order to obtain the corrected band structures of bulk and g-GaN. To compute the optical properties, the random-phase approximation (RPA) [31,32] was employed in addition to the PBE approach, using a total of 96 (valence and conduction) bands. A Monkhorst-Pack [33] k-point sampling of $127 \times 127 \times 1$ was adopted for PBE-RPA calculations of the 2D unit cell. For 3D zb- and wz-GaN structures, the k-point mesh and the number of bands were scaled accordingly.

III. 3D GaN CRYSTALS

The thermodynamically stable phase of 3D GaN crystal has a wurtzite structure, which corresponds to a global minimum. As for zb-GaN, it can form in the epitaxial growth of thin films on (011) planes of the cubic substrates [2], hence it has a slightly lower cohesive energy relative to wz-GaN.

A. Crystal structure and energetics

wz-GaN is constructed from two interpenetrating hexagonal close-packed lattices, each having two of each constituent atom, Ga or N. The structure has $P63mc$ space group symmetry, and lattice constants $a = b$ and c. zb-GaN consists of two interpenetrating fcc lattices each having four of the two atoms at the lattice points. The cubic structure has $F\bar{4}3m$ space group. Both allotropes have tetrahedral coordination for the first nearest neighbors, but they differ in the second-nearest-neighbor coordination.

In the present study, we carried out structure optimization calculations of wz-GaN and zb-GaN crystal with GGA (using only $4s$ and $4p$ valence orbitals), GGA + d (including also $4d$ orbitals), GGA − GW, and GGA + d − GW potentials; however, we prefer to display and tabulate the results only given by GGA + d potential throughout the paper, due to the reliable values given by this functional. In Fig. 1 we present atomic configurations of wz-GaN and zb-GaN in their

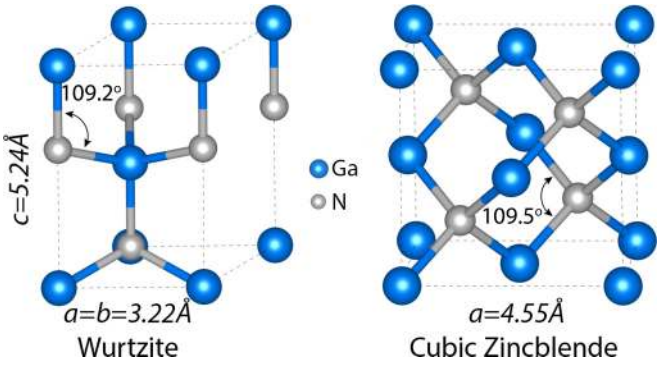

FIG. 1. Optimized atomic structures of wz-GaN and zb-GaN in their hexagonal and cubic conventional cells, respectively. Lattice constants and bond angles are indicated. Larger (blue) and smaller (gray) balls stand for Ga and N atoms.

conventional cells, which were optimized through GGA + d calculations.

For each optimized structure, we calculated the lattice constants, Ga-N bond length d, cohesive energy per Ga-N pair E_c, bulk modulus B, charge transfer from cation to anion Q_b^*, Born effective charge Z^*, and direct band gap between valence and conduction bands E_{G-d}. Our results are listed in Table I for wz-GaN and in Table II for zb-GaN. The present calculated values can be compared with values calculated by previous theoretical studies and measured experimentally presented in the same tables.

While the previous LDA calculations provides overbinding, predicting $a = 3.17$ Å and $c = 5.15$ Å, the corresponding experimental values were measured as $a = 3.19$ Å and $c = 5.19$ Å. Apparently, lattice constants of wz-GaN are underestimated by LDA calculations. The present GGA + d calculations predict $a = 3.22$ Å and $c = 5.24$ Å. In addition, the experimental value of the cohesive energy, 9.06 eV/GaN pair, is predicted here as $E_c = 8.76$ eV/GaN pair. As for the bulk modulus, the predicted value of 171 GPa is lower than the experimentally measured values between 188 and 245 GPa. Furthermore, Bader charge analysis [21] reveals that charge transfer Q_b^* from Ga to N atoms was at a value of 1.54 electrons.

For zb-GaN, GGA + d calculations provide the best predictions; the calculated value of $a = 4.55$ Å for the experimental lattice constant of $a = 4.54$ Å. As expected, the cohesive energy of zb-GaN calculated as $E_c = 8.75$ eV/pair is slightly smaller than that of wz-GaN, which can be compared with the experimental value measured as 8.90 eV/GaN pair [57]. The bulk modulus, which is calculated to be $B = 170$ GPa, is in good agreement with the experimental values reported as 185–190 GPa [56,58].

B. Electronic structure of 3D GaN crystals

In a simple tight-binding picture of the bond orbital model [59], the cation Ga having $4s^2 4p^1$ and the anion N having $2s^2 2p^3$ valence orbitals each form four sp^3 hybrid orbitals, $|h_c\rangle$ and $|h_a\rangle$, in the tetrahedral directions. The sp^3 hybrid orbital of N has lower energy than the sp^3 hybrid orbital of Ga, namely $E_{|h_c\rangle} > E_{|h_a\rangle}$. When combined to form bond orbitals $\Psi_b\rangle = (|h_c\rangle + |h_a\rangle)/\sqrt{2}$ along four tetrahedrally coordinated bonds, charge is transferred from cation to anion attributing some polar character to covalent bond orbitals. As a result, directional bond orbitals carry both polarity and covalency. According to the bond orbital model, GaN bonds have polarity $\alpha = 0.62$. In compliance with this analysis, the top of the valence band is dominated by N-2p orbital states. Eight electrons per Ga-N pair and an energy difference of $E_{|h_a\rangle}$ and $E_{|h_c\rangle}$ dictate a wide band gap of 3D GaN crystals. With the guidance of this simple analysis, we now examine the calculated electronic band structure of 3D GaN crystals.

In Fig. 2, we present the electronic band structure of wz-GaN, which was calculated within the GGA using PBE along major symmetry directions. It is a direct-band-gap semiconductor with $E_{G-d} = 1.71$ eV, which is underestimated

TABLE I. Lattice constants $a = b$ and c; c/a ratio; Ga-N bond length d, cohesive energy E_c per Ga-N pair; bulk modulus B, Poisson's ratio ν, charge transfer Q_b^* from cation to anion through Bader analysis [21], Born effective charges Z^*, and direct band gap E_{G-d} of wz-GaN crystal calculated by using PBE, HSE06 (with different mixing parameters α), and G_0W_0 approaches. For the sake of comparison, values obtained from the previous theoretical studies and experiments are also included.

	a (Å)	c (Å)	c/a	d (Å)	E_c (eV/GaN)	B (GPa)	ν (%)	Q_b^* (e)	Z^* (e)	E_{G-d} (eV)
GGA + d	3.22	5.24	1.63	1.97	8.76	171	0.18	1.54	2.63	1.71
HSE06 ($\alpha = 0.25/0.35$)										2.96/3.48
G_0W_0										3.03
LDA/GGA [34]	3.16/3.22	5.15/5.24	1.63							2.12/1.74
LDA [35]	3.14		1.63			215			2.64	
LDA [36]	3.20		1.63						2.72	
LDA [37]	3.15		1.63			195				
GGA [38]	3.19									1.83
LDA/HSE [39]	3.15/3.18	5.14/5.17	1.63						2.58/2.64	
LDA@FP-LAPW [40]	3.17	5.15	1.63			207				2.22
HSE06 [41]	3.20	5.20	1.63							3.21
HSE06 ($\alpha = 0.25/0.30$) [34]	3.18/3.17	5.17/5.16	1.63							3.27/3.48
G_0W_0@OEP$_x$(cLDA) [42]	3.19	5.19	1.63							3.24
Expt. [38,43–50]	3.19	5.19	1.63		9.06	188,195,205,237,245	0.20		2.65	3.40-3.50

TABLE II. Cubic lattice constant a; Ga-N bond length d, cohesive energy E_c per Ga-N pair; bulk modulus B, Poisson's ratio ν, charge transfer Q_b^* from cation to anion obtained by Bader analysis [21], Born effective charge Z^*, and direct band gap E_{G-d} calculated by PBE, HSE06 (with different mixing parameters α) and G_0W_0. For the sake of comparison, values obtained from the previous theoretical studies and experiments are also included.

	a (Å)	d (Å)	E_c (eV/GaN)	B (GPa)	ν (%)	Q_b^* (e)	Z^* (e)	E_{G-d} (eV)
GGA + d	4.55	1.97	8.75	170	0.34	1.52	2.68	1.55
HSE06 ($\alpha = 0.25/0.35$)								2.74/3.30
G_0W_0								2.85
LDA [37]	4.46			183				
LDA [35]	4.45			207			2.65	
GGA [51]	4.56							1.66
G_0W_0@LDA [52–55]	4.5							2.79,2.88,3.09
Expt. [44,56–58]	4.54,4.50		8.90	185–190	0.37			3.30

by 1.7 eV with respect to the reported experimental values, in the range of 3.40–3.50 eV. Our prediction agrees with the previous calculations within the GGA [34], but it is 0.4 eV smaller than that of the LDA [34]. Present and previous GGA calculations, as well as other previous calculations, are known to underestimate the fundamental band gap. Here we apply corrections to present PBE values by using HSE06 and quasiparticle GW methods. After HSE06 correction, the direct band gap of wz-GaN increases to 2.96 eV (and even to 3.48 eV when exchange parameter $\alpha = 0.35$), yet it remains ∼0.44 eV below the experimental value. The GW correction slightly opens the band gap further to 3.03 eV, which is still ∼0.37 eV smaller than the experimental gap.

The electronic energy structure of zb-GaN calculated by PBE is presented in Fig. 3. Similar to wz-GaN, zb-GaN is a direct-band-gap semiconductor with a PBE band gap $E_{G-d} = 1.55$ eV, which is 1.75 eV smaller than the experimentally measured values averaged at 3.30 eV. After HSE06 corrections, the calculated value increases to 2.74 eV, yet it is ∼0.56 eV smaller than experimental values. The G_0W_0 correction opens up the band gap further to 2.85 eV, which is still ∼0.45 eV smaller than the experimental gap. Nonetheless, the fundamental band gaps of both wz-GaN and zb-GaN can be closed further by HSE06 by tuning the exchange parameter α as 0.35, to 3.48 and 3.30 eV, respectively.

IV. 2D g-GaN

Using the LDA within DFT, a prior study addressed the question of whether IV-IV elemental and III-V and II-VI compound semiconductors can form stable 2D crystalline structures, and it was found that GaN can form a stable, planar, single-layer honeycomb structure [6–8]. In the present paper we call this structure g-GaN, and we first examine its stability, which was proven earlier by phonon calculations [6]. Here, we repeat phonon frequency calculations using the GGA, and we perform finite-temperature MD calculations in order to assure that the equilibrium structure is not a shallow minimum on the BO surface. Furthermore, we investigate the properties of g-GaN by using different methods within DFT, and we apply HSE06 corrections to the fundamental band gap. In doing so, we are able to provide a consistent comparison with 3D crystals to reveal the effect of dimensionality. In particular, we deduce

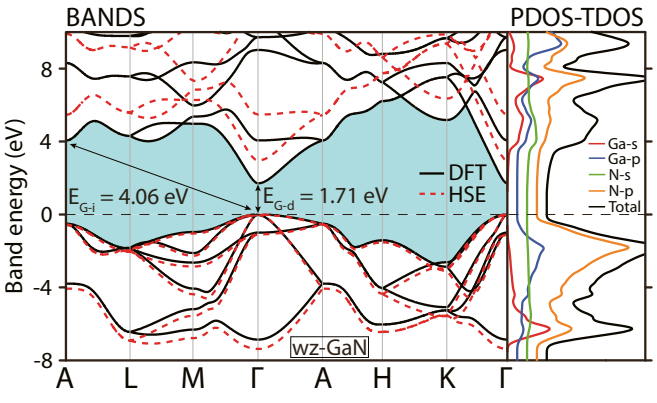

FIG. 2. Electronic energy band structure of wz-GaN calculated by PBE. The total (TDOS) and partial (PDOS) densities of states projected to valence orbitals are slightly shifted for clarity. The bands after the HSE corrections are shown by the dashed lines. The fundamental band gap of PBE calculations is shaded. The zero of energy is taken at the top of the valence band at the center of the Brillouin zone.

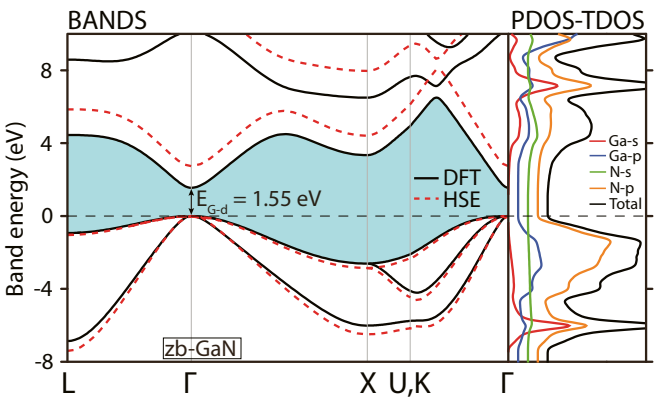

FIG. 3. Electronic energy band structure of zb-GaN calculated by PBE. TDOS and PDOSs projected to valence orbitals are shifted for clarity. The bands after the HSE corrections are shown by the dashed lines. The fundamental band gap of PBE calculations is shaded. The zero of energy is taken at the top of the valence band at the center of the Brillouin zone.

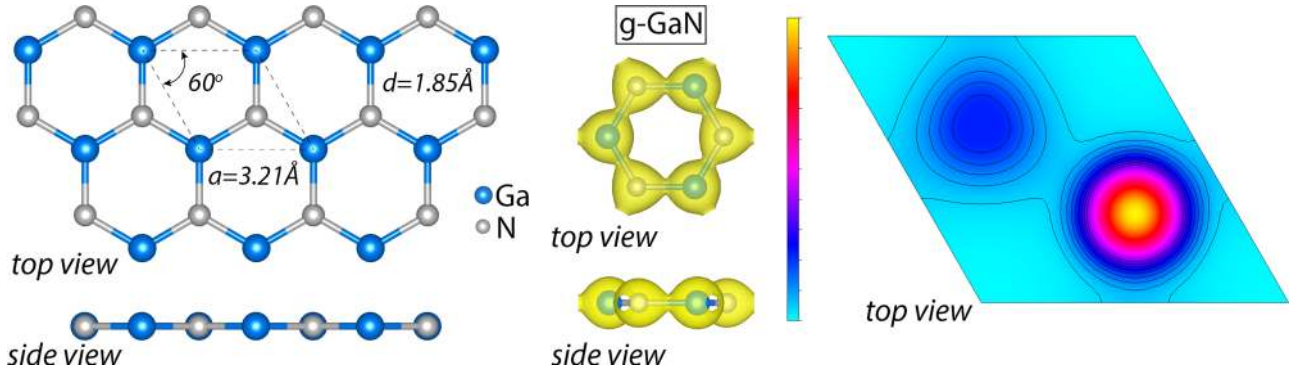

FIG. 4. Left: Top and side views of the optimized atomic structure of g-GaN. The 2D hexagonal primitive unit cell is delineated by dashed lines. The lattice constants $a = b$ and Ga-N bond length are indicated. Large (blue) and relatively smaller (gray) balls denote Ga and N atoms, respectively. Middle: Isosurfaces of the total charge density of the hexagon. Right: Charge-density contour plots of the Ga-N bond in a horizontal plane passing through the Ga-N bond and corresponding color scale. The bond charge of σ-bond is shown.

the crucial differences between the physical properties of 3D wz-, zb-GaN, and g-GaN, particularly the optical-absorption spectra.

A. Structure, energetics, and mechanical properties

In g-GaN structure, Ga-sp^2 and N-sp^2 hybrid orbitals form σ-bonds along Ga-N bonds arranged as a hexagon. Due to the planar sp^2 bonding, the bond angle between Ga-N bonds is 120°. In addition to three sp^2 hybrid orbitals of each constituent, Ga and N, their p_z orbitals are perpendicular to the plane of g-GaN. While the σ-bonds attain the strength of g-GaN, the π-bonds between nearest Ga-p_z and N-p_z orbitals maintain the planar geometry of g-GaN. It is known that graphenelike compounds are not buckled but are rather planar if one of the constituents is from the first row of the Periodic Table, such as graphene, BN, BP, and AlN monolayers with a honeycomb structure. Due to the electronic charge transfer from Ga to N, in addition to σ- and π-bonding, an ionic bonding with Madelung energy contributes to the cohesive energy.

The atomic structure of g-GaN was optimized by using the CG method. The equilibrium structure of free-standing g-GaN is a planar honeycomb structure with a 2D hexagonal lattice. The optimized atomic structure together with the primitive cell and its lattice constants are shown in Fig. 4. In the same figure, the schematic description of the bonding in compliance with the above discussion is presented. Charge-density contour plots of a Ga-N bond in a horizontal plane (in the atomic plane of g-GaN) are also shown. The isosurfaces of the total charge density mimic the electron distribution over the hexagons, where Ga and N atoms are alternatingly placed at the corners. It is noted that Ga-N bonds in 3D wz(zb)-GaN, which is constructed from tetrahedrally coordinated sp^3 hybrid orbitals, are 0.12 Å longer than the Ga-N bonds of g-GaN constructed from planar sp^2 hybrid orbitals $+p_z$ orbitals. This indicates that Ga-N bonds in g-GaN are stronger than those in wz(zb)-GaN. Despite the stronger bonding in planar g-GaN, the cohesive energy of 3D wz-GaN crystal, which is fourfold-coordinated, is 0.70 eV higher than that of g-GaN. Accordingly, g-GaN corresponds to a local minimum on the BO surface.

Lattice constants $a = b$, bond length d, cohesive energy E_c, in-plane stiffness C, charge transfer, Born effective charge values, and fundamental band gaps E_G calculated by different methods are presented in Table III. In the same table, we included results of the previous studies for the sake of comparison.

For g-GaN, our PBE calculation predicts a and d values (3.21 and 1.85 Å, respectively), which are in good agreement with previous theoretical results [6,60]. While cohesive energy per GaN pair is generally overestimated by LDA calculation, values of in-plane stiffness and Poisson's ratio agree better with

TABLE III. Optimized lattice constant a; Ga-N bond length d, cohesive energy E_c per Ga-N pair; in-plane stiffness C, Poisson's ratio ν, charge transfer Q_b^* from Ga to N, Born effective charge Z^*, and indirect band gap E_{G-i} of g-GaN.

	a (Å)	d (Å)	E_c (eV/GaN)	C (N/m)	ν (%)	Q_b^* (e)	Z^* (e)	E_{G-i} (eV)
GGA + d	3.21	1.85	8.04	109.8	0.43	1.50	3.08	2.16
HSE06 ($\alpha = 0.25/0.35$)								3.42/3.98
G_0W_0								4.55
LDA [6]	3.20	1.85	12.74	110	0.48	1.70		2.27 (GW_0: 5.0)
LDA [60]	3.21	1.85		109.4	0.43			
LDA [61]		1.85	8.38					2.17
GGA [62]		1.87	8.06					1.87 (GW_0: 4.14)
G_0W_0 [63]	3.17							4.27 (LDA: 2.36)
PBE/HSE/G_0W_0 [64]	3.25					1.34	3.23	3.23 (HSE06)/4.00 (G_0W_0)

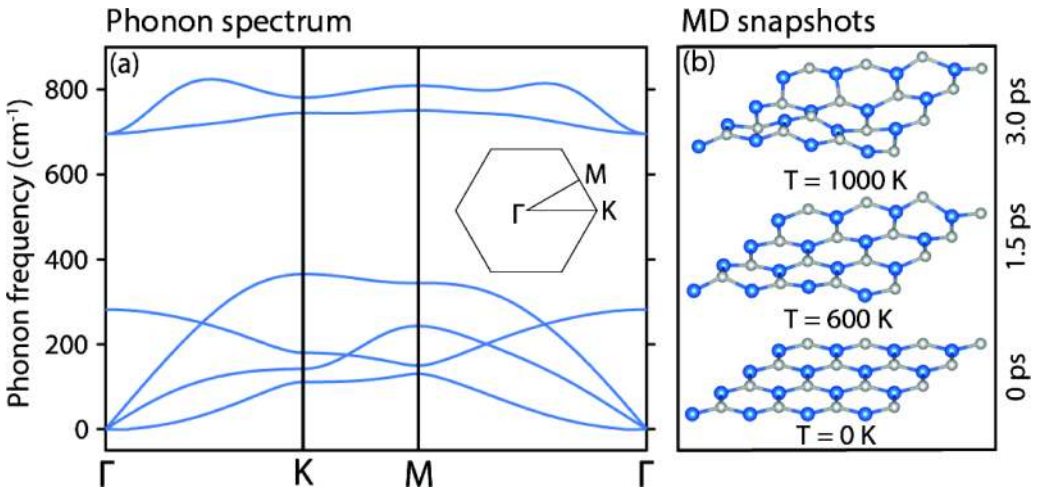

FIG. 5. (a) Calculated phonon-dispersion curves, Ω vs $\mathbf{k}$, along major symmetry directions of the Brillouin zone shown by the inset. (b) Snapshots of the atomic configurations in MD simulations at 0, 600, and 1000 K, in which honeycomb-like structures are maintained.

previous LDA calculation [6]. Finally, Bader analysis yielding a charge transfer of 1.5 electrons from Ga to N indicates significant ionic contribution in the binding.

B. Stability: Phonon spectra and MD simulations

Even if structure optimization performed using the CG method indicates equilibrium structure, it is not necessarily stable under the displacements of atoms in g-GaN. To check whether free-standing g-GaN in a honeycomb structure remains stable under the displacements of the constituent atoms, we carry out the calculations of the frequencies of crystal vibrations and determine the phonon frequency spectrum. It is well known that if the vibration frequency of specific modes, $\Omega(\mathbf{k})$, is imaginary, the corresponding displacements would result in an instability, since displacement cannot be restored. In Fig. 5(a), the calculated frequencies of phonon modes are positive and indicate stability. The phonon dispersions calculated here are similar to those calculated earlier using the LDA [6], except for some shifts of the optical branches.

Although the calculated frequencies of the phonon modes are all positive, instabilities can be induced through thermal excitations. This situation occurs when the local minimum of a given phase is shallow and the structure dissociates at low temperatures. To show that g-GaN can survive at high temperatures and is suitable for technological applications above room temperature, we carried out *ab initio* finite-temperature calculations in the temperature range from 0 to 1000 K. The honeycomb structure did not dissociate even after 3 ps simulation at 1000 K. This indicates that g-GaN is rather stable in a deep minimum on the BO surface, and hence devices fabricated from g-GaN can sustain operations above room temperature. In Fig. 5(b), we present snapshots of the atomic configurations obtained from MD simulations at different temperatures.

C. Electronic structure

Since an antibonding π^*-bond is separated from a π-bond by a significant energy, the π- and π^*-bands derived from these bonds open a significant band gap. Accordingly, g-GaN is a nonmagnetic, wide-band-gap semiconductor. In Figs. 6(a) and 6(b), the electronic energy band structure of g-GaN in the symmetry directions of the hexagonal Brillouin zone, as well as the corresponding total (TDOS) and orbital projected (PDOS) densities of states, is shown. While the maximum of the valence band occurs at the K-point, the minimum conduction band appears at the Γ-point. Accordingly, the energy bands calculated by PBE marks an indirect band gap from the K- to the Γ-point, $E_{G-i} = 2.16$ eV. This is a dramatic deviation from the bulk 3D wz(zb)-GaN, which has a PBE direct band gap of $E_{G-d} = 1.71$. Apparently, the fundamental band gap increases by 0.45 eV as one goes from three dimensions to monolayer two dimensions. While the lowest conduction band near the center of the Brillouin zone is derived from the Ga-p_z orbitals, the flatband at the maximum of the valence band along the K-M direction originates from the N-p_z orbital states. In

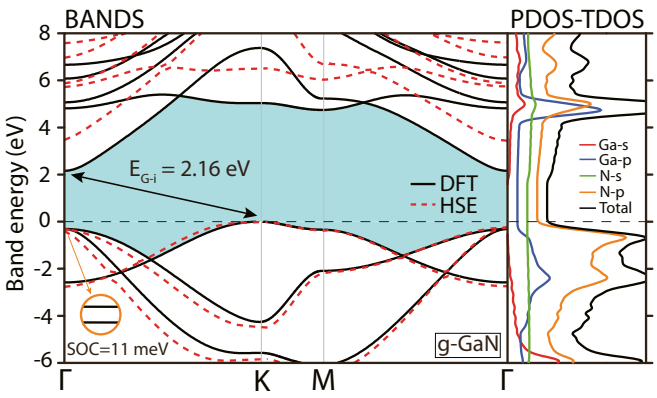

FIG. 6. The electronic energy band structure of the optimized structure of g-GaN is presented along the symmetry directions of the Brillouin zone. Zero of energy is set to the top of the valence band. The fundamental band gap between the conduction and valence bands is shaded, and the indirect band gap E_{G-i} is indicated. The splitting of the degenerate bands at the top of the valance band at the Γ-point due to spin-orbit coupling is shown by the inset. PBE bands corrected by the HSE06 method are shown by the dashed lines.

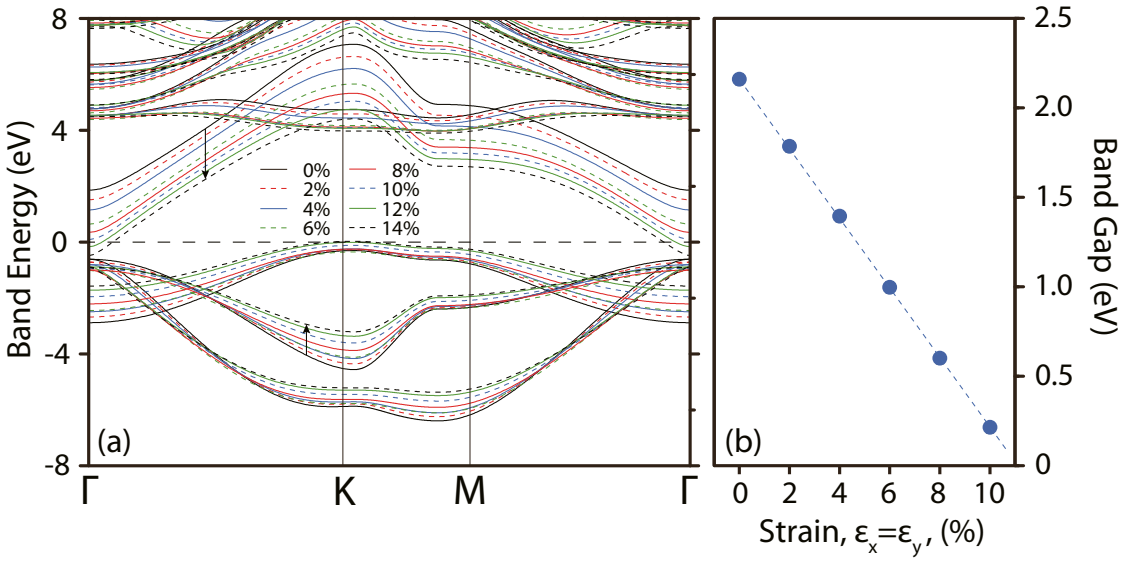

FIG. 7. (a) Variation of the energy bands of g-GaN near the fundamental band gap under applied biaxial strain $\epsilon_x = \epsilon_y = \epsilon$. (b) Variation of the minimum indirect band gap between the Γ- and K-points with applied strain.

addition to the PBE calculations of the band structure, we applied corrections by using HSE06 and G_0W_0 methods. The corrected band gaps are shown in Fig. 6. The indirect PBE band gap increased to 3.42 eV after the HSE06 correction. This corresponds to a correction of 1.26 eV. On the other hand, the correction induced by the G_0W_0 method is larger than that of the HSE06 method by nearly 1 eV, revealing a band gap of 4.55 eV. Spin-orbit coupling (SOC) at the top of the valence band at the Γ-point leads to the splitting of the degenerate bands by only 11 meV.

The response of the conduction and valence bands to the applied strain ϵ, and the resulting changes in the fundamental gap, is of interest for the fabrication of devices operating under strain. Here we examined the effect of strain on the fundamental band gap of g-GaN. Within PBE calculations, the band gap of g-GaN was found to decrease monotonically from 2.16 to 0.21 eV, going from $\epsilon = 0\%$ to 10%. Furthermore, the gap seemed to close and lead to a metallic band structure when biaxial tensile strain was further increased, up to 16%. The shifts of the conduction and valence bands under strain and the variation of the fundamental band gap are shown in Figs. 7(a) and 7(b), respectively. This is an important result predicting dramatic changes in the electronic structure with applied strain, once $\epsilon_x = \epsilon_y \leqslant 10\%$ is affordable in the g-GaN system.

As for the TDOS and the orbital projected PDOS, one also finds modifications by going from three to two dimensions. In particular, flattening of the bands near the edge of the conduction band gives rise to strong peaks in the TDOS and the PDOS. The important implications of this situation will be seen in the optical-absorption spectra in the forthcoming section.

D. Optical properties

Since wz-GaN has well-known optoelectronic applications, the investigation of the optical properties of g-GaN and their comparison with those of wz(zb)-GaN is important for future applications. In Fig. 8, we show the optical-absorption spectra of 3D wz-GaN, zb-GaN, and 2D g-GaN, all calculated using PBE-RPA approximations. Some of the critical features of these absorption spectra can be summarized as follows: (i) The onsets of the optical absorption in the imaginary dielectric function spectra $\varepsilon_2(\omega)$ are in compliance with the band gaps of these crystals calculated within PBE. In the absorption spectra of g-GaN, onset energy obtained from PBE calculations blueshifts once HSE06 corrections are applied. (ii) The sharp peak in $\varepsilon_2(\omega)$ of g-GaN occurs due to the optical transitions from flat occupied π-bands between K-

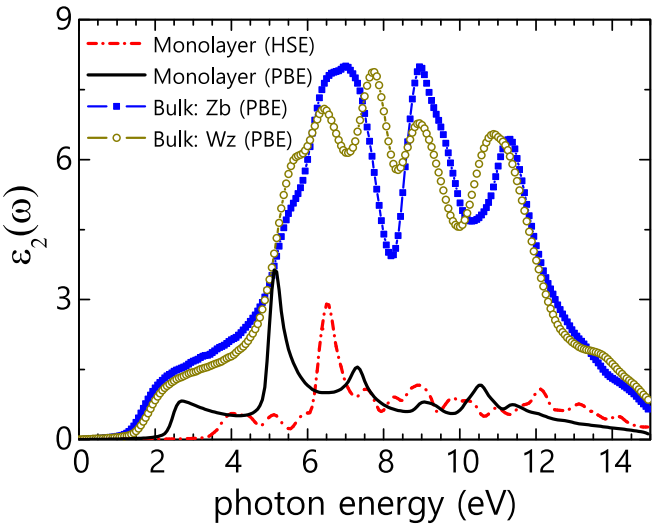

FIG. 8. Optical-absorption spectra, i.e., $\varepsilon_2(\omega)$ vs photon energy calculated for wz-GaN (light green with open circles), zb-GaN (blue with squares), and g-GaN (black solid) using the PBE-RPA approximation. The effect of HSE06 corrections on the absorption spectrum of g-GaN is shown by red dashed lines.

and M-points to flat empty π^* bands $\sim$5 eV above. This peak is blueshifted in HSE-RPA spectra by $\sim$1.5 eV. (iii) The absorption spectra of wz-GaN and zb-GaN display similar absorption onsets (below that of g-GaN) and multipeak features between 5 and 12 eV. (iv) The optical-absorption onset energy when going from 3D to 2D GaN is blueshifted, where absorption for g-GaN kicks off within the visible light region or more toward the uv range, differently from 3D wz- and zb-GaN. (v) The evident lower amplitude of the absorption spectrum of g-GaN compared to wz-GaN and zb-GaN is a well-known pattern [65] due to the weaker linear optical response of a single layer of g-GaN, normal to the incident light. This is contrary to bulk wz(zb)-GaN crystals, with periodically repeating multiples of buckled GaN planes along the direction of the lattice constant c. Hence, the optical spectra of monolayer and bulk GaN show significant differences, implying that they could be used for different optoelectronic applications. As we will discuss in the forthcoming section, the electronic properties of bilayer and multilayer structures of g-GaN undergo gradual changes with the number of layers. Therefore, one can control the optical properties by changing the number of g-GaN in the multilayer structures.

E. g-GaN on substrates

Since 3D layered GaN does not exist in nature, freestanding g-GaN cannot be exfoliated; it should be grown on a substrate. Under these circumstances, the grown overlayer and substrate can be strong, and hence the properties calculated for SL g-GaN undergo significant modifications. Here we examined the properties of a g-GaN overlayer grown on two different substrates, namely a metallic Al(111) surface and semiconducting blue phosphorene. Our models of g-GaN+substrate are presented in Fig. 9.

The Al(111) surface is rather reactive and hence can establish strong interactions with the g-GaN overlayer. In this respect, the Al(111) surface is a stringent test substrate. The Al(111) surface is represented by an Al(111) slab consisting of four Al(111) planes. Since the Al(111) surface is not lattice-matched to g-GaN, we elongated the Al(111) lattice by 15%. This allows us to treat the g-GaN+substrate system using periodic boundary conditions. Since Al-Al interaction decreases upon elongation, the reactivity of the Al atom surface can increase to enhance overlayer-substrate interaction. In this way, our test is realized in even more severe conditions. We checked three possible configurations, where (i) Ga and N

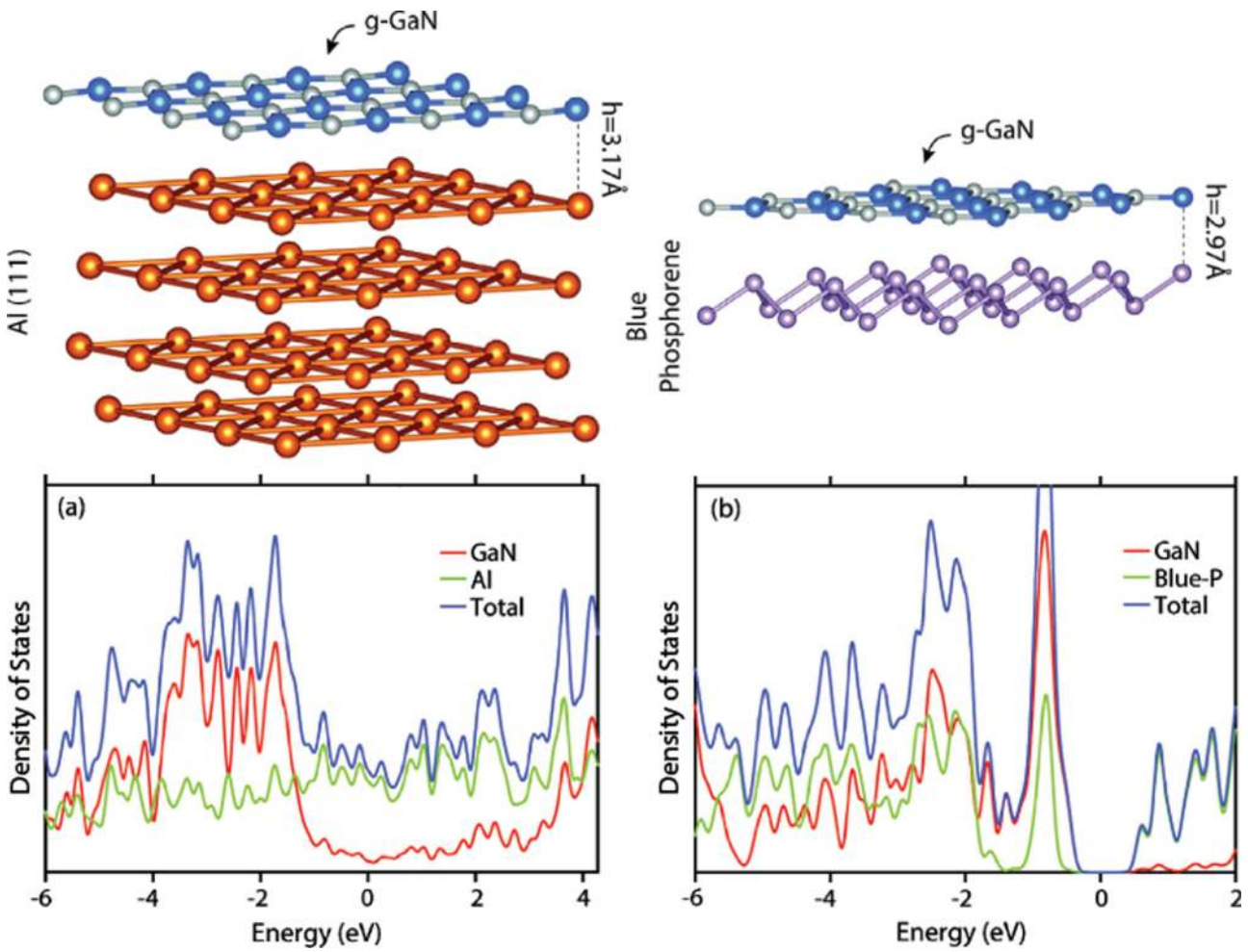

FIG. 9. (a) Optimized atomic structure of the g-GaN overlayer on Al(111) slab represented by four Al(111) atomic planes. Calculated total and local densities of states on the overlayer as well as on the Al(111) slab. (b) Optimized atomic structure of the g-GaN overlayer on a SL blue phosphorene. Calculated total and local densities of states on the overlayer as well as on SL blue phosphorene.

atoms are located above the center of hexagons, (ii) Ga atoms are on top of Al atoms, and (iii) N atoms are on top of Al atoms. Similar results are obtained for all cases, thus only case (iii) is discussed. The effect of Al(111) substrate on g-GaN is analyzed by determining the height of g-GaN from the substrate and by calculating the density of states localized on the overlayer. In Fig. 9(a), the optimized height $h = 3.17$ Å, which is larger than the sum of the covalent atomic radii of either $r_{Ga} + r_N = 1.76$ Å or $r_N + r_{Al} = 1.76$ Å [66]. The common Fermi level is shifted up by ~1 eV from the top of the valence band of g-GaN. The density of states projected onto the g-GaN overlayer is reminiscent of the state density presented in Fig. 6 with peaks $-1 < E < -2$ eV and $-3 < E < -4$ eV. Low densities of states in the gap region of g-GaN for energies $-1 < E < 1.5$ eV are partly due to numerical accuracy and weak substrate-overlayer interaction.

Interestingly, blue phosphorene, i.e., the SL buckled honeycomb structure of phosphorus, is nearly lattice-matched to g-GaN and hence is an ideal substrate to examine substrate-overlayer interaction. While we consider a single layer of blue phosphorene in order to examine its interaction with g-GaN, the same interaction with multilayer phosphorene or layered 3D blue phosphorus is not expected to change in any essential manner due to the weak vdW interlayer interaction within phosphorene. However, because of the semiconducting surface and its lattice constants nearly matching to g-GaN, 3D layered blue phosphorene appears to be an ideal substrate to grow single and multilayer structures of g-GaN. In Fig. 6(b), the height of the g-GaN overlayer from the blue phosphorene surface is $h = 2.97$ Å, which is rather large and is larger than the sums of covalent radii $r_{Ga} + r_P = 2.36$ Å. The density of states projected onto g-GaN is similar to that in Fig. 6 with the peaks at ~ -1, -2.5, and -6 eV. The fundamental band gap of the g-GaN+phosphorene system partly overlaps with that of g-GaN, whereas the conduction bands of blue phosphorene occur in the upper energy region of the g-GaN overlayer. Briefly, the density-of-states analysis suggests that the interaction between overlayer g-GaN and the underlying blue phosphorene is minute and does not allow any significant modification of the electronic structure of the freestanding g-GaN.

V. GaN BILAYER AND MULTILAYER STRUCTURES

Previous studies have shown that the physical properties of bilayer and multilayer SL honeycomb structures vary slowly [67,68]. Like SL structures, bilayer and multilayer correspond to local minima on the BO surface. Growth of multilayers as well as the 3D periodic structure allow us to construct artificial materials with novel properties such as van der Waals solids [69]. We explored this aspect of g-GaN and revealed its properties. Of course, we started by determining the most energetic stacking sequence, since there are a few stacking configurations. Here are the stacking sequences (and their optimized cohesive energies per Ga-N pair) for bilayer GaN, i.e., b-GaN: AA' (i.e., hexagons on top of each other, with the Ga atom being above N) ($E_C = 8.57$ eV); AA (Ga on Ga) ($E_C = 8.29$ eV); AB (GaN) (Bernal type, Ga above N) ($E_C = 8.49$ eV); and AB (NN), which is equivalent to AB (GaGa) ($E_C = 8.40$ eV). Accordingly, the AA' sequence is found to be energetically favorable. The total interlayer interaction is only 280 meV, where 120 meV of it is chemical interaction and the remaining 160 meV has vdW character. A similar analysis has been performed for several types of stacking sequences of trilayer GaN (t-GaN), and it was found that the sequence that is energetically most favorable is $AA'A$, with cohesive energy $E_C = 8.69$ eV per Ga-N pair. Here the cohesive energy is larger than that of g-GaN and b-GaN due to the increasing interlayer interaction. Note that in the cohesive energy calculation of wz- and zb-GaN, the vdW interaction is not taken into account within 3D bulk structures. Therefore, the bulk cohesive energies are slightly underestimated relative to those of the multilayer structures. The average interlayer interaction energy is 200 meV. The cohesive energies calculated for b- and t-GaN are in agreement with those of Xu *et al.* [61]. The extension of b- and t-GaN is the formation of multilayer m-GaN or 3D layered p-GaN, which is periodic in the direction perpendicular to the atomic planes. We carried out calculations for the structure optimization of p-GaN. We found the stacking sequence $AA'AA'\ldots$ to be energetically most favorable with $E_C = 8.94$ eV per Ga-N pair.

Having determined the most energetic stacking sequence, we next tested the stability of b-GaN. Normally, if the interlayer distance is larger than the Ga-N bond distance and the interaction among them is weak, the stability is strengthened in b-GaN. The calculation of the phonon frequencies presented in Fig. 10 demonstrates the stability of b-GaN, hence this conjecture was confirmed.

Finally, the calculated electronic structures of b-, t-, and p-GaN are presented in Fig. 11, together with their optimized structures with structural parameters, such as interlayer spacing h and lattice constants $a = b$ (c). The indirect band gap of g-GaN decreases to 1.98 eV in b-GaN and to 1.83 eV in t-GaN. Interlayer spacing h also shows this trend where it decreases with the number of layers increasing, since the total interlayer interaction also increases. However, bond lengths and lattice constants display the opposite trend.

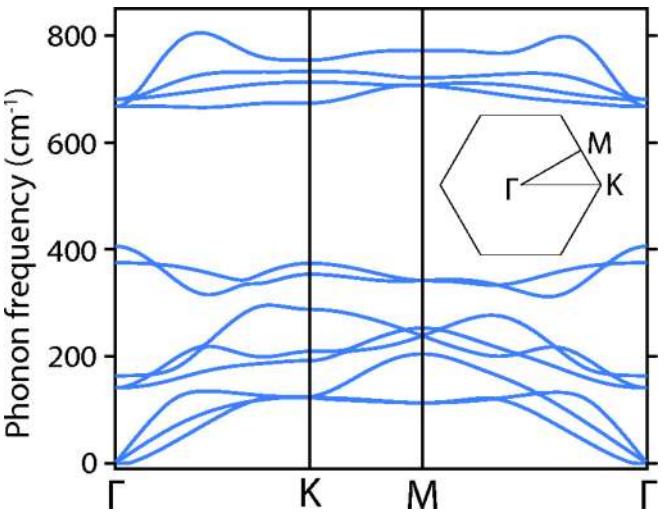

FIG. 10. Phonon-dispersion curves calculated for the bilayer of g-GaN.

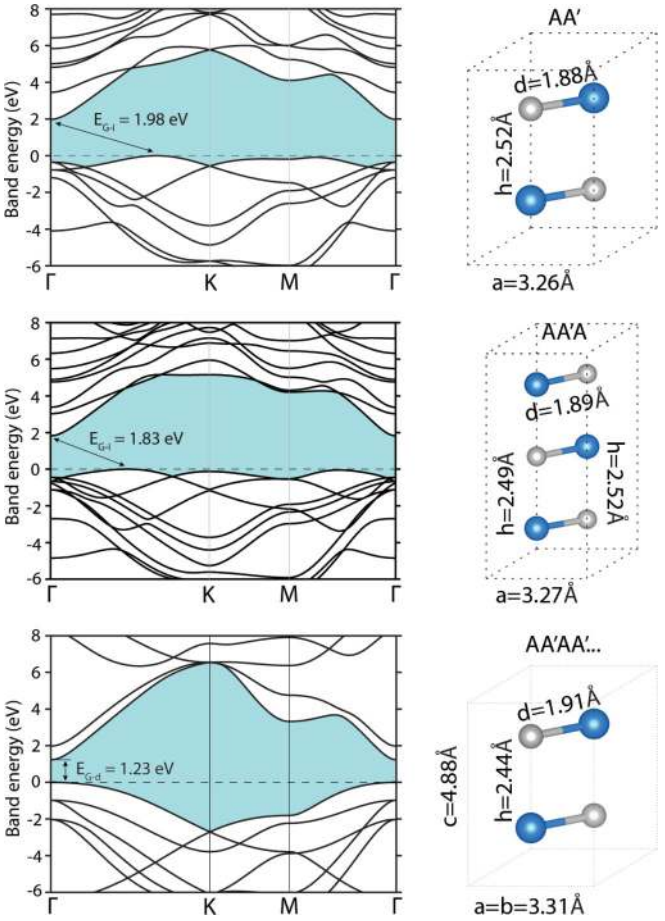

FIG. 11. Construction of van der Waals solids by g-GaN. (a) Left: energy band structure of bilayer b-GaN calculated using PBE with AA' stacking. Right: optimized atomic configuration. (b) Same as (a) for trilayer t-GaN with $AA'A$. (c) Same as (a) for 3D periodic layered structure p-GaN with $AA'AA'\ldots$ stacking. The primitive unit cell is delineated by dashed lines. Zero of energy is set to the top of the valence bands. Fundamental band gaps are shown by arrows.

In p-GaN, the total interlayer interaction is maximized. An important outcome of this study is that, as the number of layers increases, the fundamental band gap of g-GaN decreases from 2.26 to 1.98 eV in b-GaN and to 1.83 eV in t-GaN. These three band gaps are indirect. However, in p-GaN, the fundamental band gap decreases to 1.23 eV and changes from indirect to direct, as in 3D wz- and zb-GaN. The crossover from indirect to direct is expected to occur in multilayer structures having fewer than 10 layers. It is important to note that just like 3D wz- and zb-GaN, 3D p-GaN has a direct band gap, but the band gap of this predicted structure is smaller by $\sim$0.5 eV.

VI. CONCLUSIONS

In conclusion, in this paper we present an extensive comparative study of 3D bulk GaN crystals and 2D graphenelike single-layer honeycomb g-GaN, as well as its multilayer van der Waals solids carried out using first-principles DFT methods. While DFT provides predictions on the atomic structure, lattice constants, cohesive energy, and elastic properties of 3D wz-GaN and zb-GaN crystals, it underestimates the experimentally determined fundamental band gaps by 1.5–2 eV. Here we placed an emphasis on the energetics and electronic structures by applying state-of-the-art methods in order to improve their band gaps. For g-GaN, we performed high-temperature *ab initio* MD simulations showing that the stability deduced by *ab initio* phonon calculations does not correspond to a shallow minimum, but the structure resists thermal excitations by remaining stable at high temperatures. We also found that by going from 3D to 2D g-GaN, the band gap increases and is converted from direct to indirect. Additionally, state distribution in the conduction band exhibits significant changes relative to 3D wz-GaN and zb-GaN crystals. This situation is reflected in the absorption spectrum of 2D g-GaN, which is blueshifted and displays dramatic differences at higher photon energies. Finally, we found that the interaction between g-GaN and specific metallic and semiconducting substrates is weak and allows the physical properties predicted for the freestanding g-GaN to be preserved once g-GaN is grown on such substrates. In particular, blue phosphorene is nearly lattice-matched to g-GaN, which can set weak chemical and van der Waals interactions. Accordingly, layered blue phosphorus can serve as an excellent substrate to grow single-layer or multilayer g-GaN. We hope that the present work will provide helpful insights for growing g-GaN.

ACKNOWLEDGMENTS

The calculations were performed at TUBITAK ULAKBIM, High Performance and Grid Computing Center (TR-Grid e-Infrastructure). This work was supported by the Scientific and Technological Research Council of Turkey (TUBITAK) under Project No 115F088. E.D. acknowledges support from The Turkish Academy of Sciences–Outstanding Young Scientists Award Program (TUBA-GEBIP). S.C. acknowledges financial support from the Turkish Academy of Sciences (TUBA).

[1] S. Nakamura, Rev. Mod. Phys. **87**, 1139 (2015).
[2] H. Morkoc, *Handbook of Nitride Semiconductors and Devices* (Wiley-VCH Verlag, Weinheim, 2008), Vol. 1.
[3] E. Durgun, S. Tongay, and S. Ciraci, Phys. Rev. B **72**, 075420 (2005).
[4] S. Cahangirov, M. Topsakal, E. Akturk, H. Sahin, and S. Ciraci, Phys. Rev. Lett. **102**, 236804 (2009).
[5] S. Cahangirov, M. Topsakal, and S. Ciraci, Phys. Rev. B **81**, 195120 (2010).
[6] H. Sahin, S. Cahangirov, M. Topsakal, E. Bekaroglu, E. Akturk, R. T. Senger, and S. Ciraci, Phys. Rev. B **80**, 155453 (2009).
[7] E. Bekaroglu, M. Topsakal, S. Cahangirov, and S. Ciraci, Phys. Rev. B **81**, 075433 (2010).
[8] M. Topsakal, S. Cahangirov, E. Bekaroglu, and S. Ciraci, Phys. Rev. B **80**, 235119 (2009).
[9] P. Vogt, P. De Padova, C. Quaresima, J. Avila, E. Frantzeskakis, M. C. Asensio, A. Resta, B. Ealet, and G. Le Lay, Phys. Rev. Lett. **108**, 155501 (2012).

[10] P. De Padova, C. Quaresima, C. Ottaviani, P. M. Sheverdyaeva, P. Moras, C. Carbone, D. Topwal, B. Olivieri, A. Kara, H. Oughaddou, B. Aufray, and G. Le Lay, Appl. Phys. Lett. **96**, 261905 (2010).

[11] P. Tsipas, S. Kassavetis, D. Tsoutsou, E. Xenogiannopoulou, E. Golias, S. A. Giamini, C. Grazianetti, D. Chiappe, A. Molle, M. Fanciulli, and A. Dimoulas, Appl. Phys. Lett. **103**, 251605 (2013).

[12] M. Gajdoš, K. Hummer, G. Kresse, J. Furthmüller, and F. Bechstedt, Phys. Rev. B **73**, 045112 (2006).

[13] G. Kresse and J. Hafner, Phys. Rev. B **47**, 558 (1993).

[14] G. Kresse and J. Hafner, Phys. Rev. B **49**, 14251 (1994).

[15] G. Kresse and J. Furthmüller, Comput. Mater. Sci. **6**, 15 (1996).

[16] G. Kresse and J. Furthmüller, Phys. Rev. B **54**, 11169 (1996).

[17] J. P. Perdew, K. Burke, and M. Ernzerhof, Phys. Rev. Lett. **77**, 3865 (1996).

[18] J. P. Perdew, K. Burke, and M. Ernzerhof, Phys. Rev. Lett. **78**, 1396 (1997).

[19] S. J. Grimme, Comput. Chem. **27**, 1787 (2006).

[20] T. Bucko, J. Hafner, S. Lebegue, and J. G. Angyan, J. Phys. Chem. A **114**, 11814 (2010).

[21] E. Sanville, S. D. Kenny, R. Smith, and G. Henkelman, J. Comput. Chem. **28**, 899 (2007).

[22] D. Alfe, Comput. Phys. Commun. **180**, 2622 (2009).

[23] S. Baroni, S. de Gironcoli, A. Dal Corso, and P. Giannozzi, Rev. Mod. Phys. **73**, 515 (2001).

[24] S. Nosé, J. Chem. Phys. **81**, 511 (1984).

[25] J. Paier, M. Marsman, K. Hummer, G. Kresse, I. C. Gerber, and J. G. Angyan, J. Chem. Phys. **124**, 154709 (2006).

[26] J. Heyd, G. E. Scuseria, and M. Ernzerhof, J. Chem. Phys. **118**, 8207 (2003); **124**, 219906 (2006).

[27] J. Heyd and G. E. Scuseria, J. Chem. Phys. **120**, 7274 (2004); **121**, 1187 (2004).

[28] L. Hedin, Phys. Rev. **139**, A796 (1965).

[29] M. S. Hybertsen and S. G. Louie, Phys. Rev. B **34**, 5390 (1986).

[30] M. Shishkin and G. Kresse, Phys. Rev. B **74**, 035101 (2006).

[31] D. Bohm and D. Pines, Phys. Rev. **82**, 625 (1951); **85**, 338 (1952); **92**, 609 (1953).

[32] H. Ehrenreich and M. H. Cohen, Phys. Rev. **115**, 786 (1959).

[33] H. J. Monkhorst and J. D. Pack, Phys. Rev. B **13**, 5188 (1976).

[34] Q. Yan, P. Rinke, A. Janotti, M. Scheffler, and C. G. Van de Walle, Phys. Rev. B **90**, 125118 (2014).

[35] K. Karch, J. M. Wagner, and F. Bechstedt, Phys. Rev. B **57**, 7043 (1998).

[36] F. Bernardini, V. Fiorentini, and D. Vanderbilt, Phys. Rev. B **56**, R10024(R) (1997).

[37] F. Bechstedt, U. Grossner, and J. Furthmuller, Phys. Rev. B **62**, 8003 (2000).

[38] M. Magnuson, M. Mattesini, C. Hoglund, J. Birch, and L. Hultman, Phys. Rev. B **81**, 085125 (2010).

[39] M. A. Caro, S. Schulz, and E. P. O'Reilly, Phys. Rev. B **88**, 214103 (2013).

[40] Z. Dridi, B. Bouhafs, and P. Ruterana, Semicond. Sci. Technol. **18**, 850 (2003).

[41] J. Heyd, J. E. Peralta, G. E. Scuseria, and R. L. Martin, J. Chem. Phys. **123**, 174101 (2005).

[42] P. Rinke, M. Winkelnkemper, A. Qteish, D. Bimberg, J. Neugebauer, and M. Scheffler, Phys. Rev. B **77**, 075202 (2008).

[43] H. Schulz and K. H. Thiemann, Solid State Commun. **23**, 815 (1977).

[44] I. Vurgaftman and J. R. Meyer, J. Appl. Phys. **94**, 3675 (2003).

[45] H. Xia, Q. Xia, and A. L. Ruoff, Phys. Rev. B **47**, 12925 (1993).

[46] M. Ueno, M. Yoshida, A. Onodera, O. Shimomura, and K. Takemura, Phys. Rev. B **49**, 14 (1994).

[47] P. Perlin, C. Jauberthie-Carillon, J. P. Itie, A. San Miguel, I. Grzegory, and A. Polian, Phys. Rev. B **45**, 83 (1992).

[48] C. Bungaro, K. Rapcewicz, and J. Bernholc, Phys. Rev. B **61**, 6720 (2000).

[49] A. F. Wright and J. S. Nelson, Phys. Rev. B **50**, 2159 (1994); **51**, 7866 (1995).

[50] A. Polian, M. Grimsditch, and I. Grzegory, J. Appl. Phys. **79**, 3343 (1996).

[51] Y. Du, B. Chang, X. Fu, X. Wang, and M. Wang, Optik **123**, 2208 (2012).

[52] X.-Z. Li, R. Gomez-Abal, H. Jiang, C. Ambrosch-Draxl, and M. Scheffler, New J. Phys. **14**, 023006 (2012).

[53] T. Kotani and M. van Schilfgaarde, Solid State Commun. **121**, 461 (2002).

[54] M. Rohlfing, P. Kruger, and J. Pollmann, Phys. Rev. B **57**, 6485 (1998).

[55] P. Rinke, A. Qteish, J. Neugebauer, C. Freysoldt, and M. Scheffler, New J. Phys. **7**, 126 (2005).

[56] M. E. Sherwin and T. J. Drummond, J. Appl. Phys. **69**, 8423 (1991).

[57] R. C. Weast, *CRC Handbook of Chemistry and Physics* (CRC, Boca Raton, FL, 1988).

[58] G. Ramirez-Flores, H. Navarro-Contreras, A. Lastras-Martinez, R. C. Powell, and J. E. Greene, Phys. Rev. B **50**, 8433 (1994).

[59] W. A. Harrison and S. Ciraci, Phys. Rev. B **10**, 1516 (1974); S. Ciraci, I. P. Batra, and W. A. Tiller, *ibid.* **12**, 5811 (1975).

[60] Q. Peng, C. Liang, W. Ji, and S. De, Appl. Phys. A **113**, 483 (2013).

[61] D. Xu, H. He, R. Pandey, and S. P. Karna, J. Phys.: Condens. Matter **25**, 345302 (2013).

[62] Q. Chen, H. Hu, X. Chen, and J. Wang, Appl. Phys. Lett. **98**, 053102 (2011).

[63] C. Attaccalite, A. Nguer, E. Cannuccia, and M. Gruning, Phys. Chem. Chem. Phys. **17**, 9533 (2015).

[64] H. L. Zhuang, A. K. Singh, and R. G. Hennig, Phys. Rev. B **87**, 165415 (2013).

[65] D. Kecik, C. Bacaksiz, R. T. Senger, and E. Durgun, Phys. Rev. B **92**, 165408 (2015).

[66] C. Kittel, *Introduction to Solid State Physics* (Wiley, New York, 2004).

[67] S. Cahangirov, V. O. Ozcelik, L. Xian, J. Avila, S. Cho, M. C. Asensio, S. Ciraci, and A. Rubio, Phys. Rev. B **90**, 035448 (2014).

[68] S. Cahangirov, V. O. Ozcelik, A. Rubio, and S. Ciraci, Phys. Rev. B **90**, 085426 (2014).

[69] A. K. Geim and I. V. Grigorieva, Nature (London) **499**, 7459 (2013).